processes

Article

Adaptive Enhancement of Thermal Infrared Images for High-Voltage Cable Buffer Layer Ablation

Hao Zhan [1,2], Jing Zhang [1,2], Yuhao Lan [3,*], Fan Zhang [4,*], Qinqing Huang [1,2], Kai Zhou [3] and Chengde Wan [1,2]

[1] State Grid Electric Power Research Institute, Nanjing 211006, China; blues_zh@hotmail.com (H.Z.); narizhangjing@foxmail.com (J.Z.); huangqq934@foxmail.com (Q.H.); wanchengdee@163.com (C.W.)
[2] Wuhan NARI Limited Liability Company of State Grid Electric Power Research Institute, Wuhan 430074, China
[3] College of Electrical Engineering, Sichuan University, Chengdu 610065, China; zhoukai_scu@163.com
[4] College of Electronics and Information Engineering, Sichuan University, Chengdu 610065, China
* Correspondence: lyh000415@163.com (Y.L.); fan.zhang@scu.edu.cn (F.Z.)

Abstract: In recent years, ablation of the buffer layer in high-voltage cables has become a prevalent issue compromising the reliability of power transmission systems. Given the internal location of these faults, direct monitoring and assessment are challenging, resulting in numerous undetected ablation hazards. Previous practice has demonstrated that detecting buffer layer ablation through surface temperature distribution changes is feasible, offering a convenient, efficient, and non-destructive approach. However, the variability in heat generation and the subtle temperature differences in thermal infrared images, compounded by noise interference, can impair the accuracy and timeliness of fault detection. To overcome these challenges, this paper introduces an adaptive enhancement method for the thermal infrared imaging of high-voltage cable buffer layer ablation. The method involves an Average Gradient Weighted Guided Filtering (AGWGF) technique to decompose the image into background and detail layers, preventing noise amplification during enhancement. The background layer, containing the primary information, is enhanced using an improved Contrast Limited Adaptive Histogram Equalization (CLAHE) to accentuate temperature differences. The detail layer, rich in high-frequency content, undergoes improved Adaptive Bilateral Filtering (ABF) for noise reduction. The enhanced background and detail layers are then fused and stretched to produce the final enhanced thermal image. To vividly depict temperature variations in the buffer layer, pseudo-color processing is applied to generate color-infrared thermal images. The results indicate that the proposed method's enhanced images and pseudo-colored infrared thermal images provide a clearer and more intuitive representation of temperature differences compared to the original images, with an average increase of 2.17 in information entropy and 8.38 in average gradient. This enhancement facilitates the detection and assessment of buffer layer ablation faults, enabling the prompt identification of faults.

Keywords: high-voltage cable; buffer layer; ablation fault; thermal infrared image; image enhancement

Citation: Zhan, H.; Zhang, J.; Lan, Y.; Zhang, F.; Huang, Q.; Zhou, K.; Wan, C. Adaptive Enhancement of Thermal Infrared Images for High-Voltage Cable Buffer Layer Ablation. *Processes* **2024**, *12*, 2543. https://doi.org/10.3390/pr12112543

Academic Editor: Mohd Azlan Hussain

Received: 8 October 2024
Revised: 4 November 2024
Accepted: 9 November 2024
Published: 14 November 2024

1. Introduction

High-voltage cables, as a key equipment for power transmission, play a crucial role in achieving long-distance, high-efficiency energy distribution and ensuring the stable operation of modern society. High-voltage cable lines that have been in operation since 2000 have been in service for a considerable period. As the usage time increases, they are affected by complex environments, leading to potential dangers and faults such as insulation aging, which gradually become apparent. These issues can cause the cable structure to be damaged and render it inoperable. Therefore, monitoring and analyzing potential hazards and faults is of great significance for ensuring the stable and reliable operation of the cables [1–3].

Buffer layer ablation has become a frequent high-voltage cable fault in recent years, causing serious negative impacts on the safe operation of power transmission systems and attracting widespread attention from both academia and industry [4–6]. For the normal operation of high-voltage cables, as shown in Figure 1, the buffer layer plays a crucial role in the cross-sectional diagram, including maintaining good electrical contact between the insulation shielding layer and the aluminum sheath, uniform electric field distribution, cushioning mechanical stress, and absorbing moisture. However, it has been observed in practice that the buffer layer is a common site for faults, with typical examples being buffer layer ablation faults, mainly occurring in cables after five years of operation. Since these faults are internal to the cable and difficult to directly monitor and assess, a large number of ablation hazards cannot be discovered and addressed in a timely manner. Figure 2 shows the dissection of a cable with a buffer layer ablation accident. White spots can be observed on the buffer layer, with the presence of white substances on the surface, and corresponding corrosion pits appear on the aluminum sheath [7]. To gain a deeper understanding of buffer layer ablation faults, experts and scholars have conducted research on the causes of these phenomena and the underlying mechanisms from different perspectives.

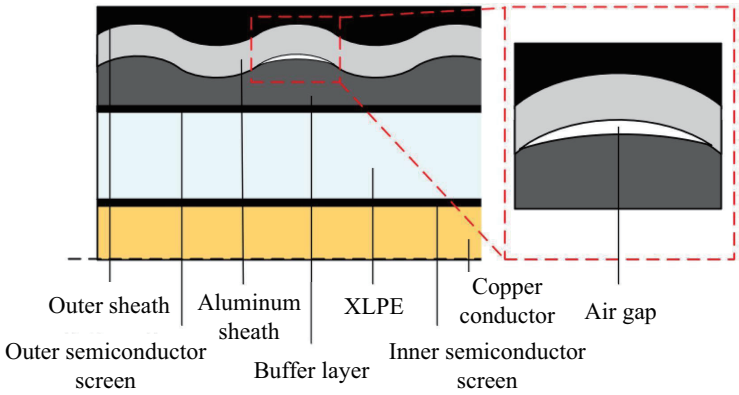

Figure 1. High-voltage cable longitudinal cross-sectional view.

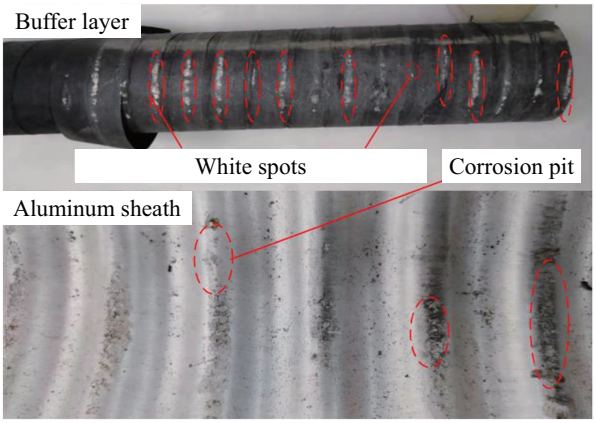

Figure 2. Buffer layer ablation fault cable dissection diagram.

Based on the results of simulated experiments and the faulted cable, Liu et al. [8] identified sodium bicarbonate as the primary component of white spots resulting from the chemical reaction between the aluminum sheath and the water-blocking powder under a humid condition. Chen et al. [9] investigated the failure characteristics and phenomena within buffer layers, such as white spots and ablated traces. Their experiments indicated that water was the primary agent in the formation of white spots and the electrochemical corrosion of the aluminum sheath. Hui et al. [10] found that moisture and the aluminum sheath are the critical factors in white-spot formation, with pressure and current acting

as accelerants. The simulation results by Jiang et al. [11] indicated that poor contact between the corrugated aluminum sheath and the buffer layer can initiate discharges, which were identified as a contributing factor to ablation. Song et al. [4] analyzed a typical ablation failure case and revealed that both the volume resistivity and water content exceeded the existing standards. Xin et al. [12] concluded that heat aging induced by circulating currents in the metal sheath could be a contributing factor to the aging ablation. Zhang et al. [13] found that higher overvoltage frequencies result in increased resistance heating and elevated temperatures surrounding the white-spot buffer layer, potentially leading to ablation due to electric heating. Recently, Zhang et al. [5] explored the impact of buffer layer structural inhomogeneity on ablation failure, revealing that inhomogeneous fiber protrusions can trigger air gap breakdowns within cables. Tian et al. [6] developed an integrated analysis framework to elucidate the comprehensive mechanisms of ablation failure in high-voltage cable buffer layers. The aforementioned work on the causes and mechanisms of buffer layer ablation faults can provide reference for condition monitoring, evaluation, and optimization of the buffer layer structure.

Automated defect detection and status evaluation have received widespread attention in different fields in recent years [14–20]. Scholars have also explored methods for assessing and monitoring the ablation status of buffer layers in order to detect faults at an earlier stage. Wu et al. [21] developed a model to calculate voltage distribution, which aids in analyzing discharge defects within the buffer layer of high-voltage cables. Their model integrated the influence of air gaps and white spots between the aluminum sheath and buffer layer on the internal voltage distribution of the cables. The study's findings indicated that the susceptibility to discharge in the buffer layer can be quantitatively evaluated based on the characteristics of white-spot defects. Liu et al. [22] investigated the advanced processing of power cable X-ray digital images and the intelligent identification of buffer layer defects. They proposed employing a fully convolutional neural network (FCNN) for the intelligent recognition of defects in the buffer layer of power cables. Huang et al. [23] employed terahertz time-domain measurements and commercial computed tomography (CT) to identify ablation defects within the buffer layer. They encountered challenges in detecting internal defects using terahertz time-domain measurements due to the sheath's impermeability to terahertz wave energy. In contrast, commercial CT scans can identify defects of varying densities within the buffer layer. He et al. [24] conducted research on the acoustic characteristics of the buffer layer to further explore the potential of acoustic detection methods. They developed a numerical acoustic model that accounts for the porous characteristics and structural attributes of the buffer layer. This model facilitated the determination of the propagation characteristics of acoustic signals resulting from buffer layer discharges and the assessment of the applicability of ultrasonic detection techniques. Chen et al. [7] assessed the corrosion rate by quantifying the hydrogen gas release and investigated the distinct functions of sodium polyacrylate (NaPA) in the corrosion process. Their findings revealed that the complexation reactions between NaPA and aluminum not only mitigated corrosion but also enhanced the buffer layer's electrical resistance. Liu et al. [25] suggested a method for diagnosing buffer layer ablation faults using frequency domain impedance spectroscopy coupled with artificial intelligence. They utilized the frequency domain amplitude spectroscopy data from buffer layer ablation and local aging faults as datasets for training and validating a neural network model, enabling the identification of such faults.

Overall, these methods are of great significance for the status assessment of buffer layers, but they have some limitations. For example, the X-ray detection method requires multiple adjustments of the detector and the radiation source during the detection, and X-rays have certain hazards, making it difficult to apply them to large-scale field detection. The gas analysis method requires drilling into the cable to collect gas and using a chromatograph to analyze the gas composition, which is somewhat destructive and operationally complex. In comparison, the scheme to assess buffer layer ablation faults by detecting changes in the surface temperature distribution of high-voltage cables has the advantages

of simple operation and non-destructiveness. Such methods are more in line with the needs of practical applications and have been studied and applied in other types of power system fault monitoring [26–28]. However, the core challenge faced by this method is the varying degree of heat generation caused by buffer layer ablation faults, sometimes with a low temperature rise, around 1 degree Celsius, leading to an inconspicuous visual representation of temperature differences on thermal infrared images and interference from noise, affecting the timeliness and accuracy of ablation status monitoring and assessment. Therefore, there is an urgent need for an algorithm that can enhance the thermal infrared images of high-voltage cables to more intuitively reflect temperature differences or changes, facilitating the effective detection of buffer layer ablation defects. Although there are already spatial domain image enhancement methods such as histogram equalization and frequency domain image enhancement methods such as non-subsampled contourlet transform [29–31], the enhancement effect is not ideal for high-voltage cable thermal infrared images with low contrast and noise interference. How to enhance detail differences while suppressing noise is the main challenge faced.

In response to the aforementioned issues and considering the characteristics of high-voltage cable infrared thermal images, this paper proposes an effective adaptive enhancement method for infrared thermal images of buffer layer ablation in high-voltage cables, enabling the prompt identification of faults. The main contributions are summarized as follows:

- To avoid amplifying noise during the enhancement process, we propose Average Gradient Weighted Guided Filtering (AGWGF) for image background and detail layer decomposition.
- To highlight temperature differences or changes, we propose an improved Contrast Limited Adaptive Histogram Equalization (CLAHE) for the background layer.
- To suppress noise interference, we propose an improved Adaptive Bilateral Filtering (ABF) for the detail layer.
- Experiments demonstrate that the enhanced results can more clearly and intuitively reflect temperature differences, which is beneficial for the monitoring of ablation faults.

2. Experimental Materials and Test Images

In this study, a section of ZC-YJLW03 64/110 high-voltage cable was used as an experimental sample, and fault defects were simulated. A voltage regulator was used to gradually increase the voltage between the aluminum sheath and the outer semi-conductive layer to 80 V. During this process, an HIKMICRO infrared thermal imager was used to record a sequence of cable infrared images that reflect temperature changes, which served as experimental test data. In this experiment, nine images were selected from the sequence as test images, as shown in Figure 3. It can be observed that the directly collected thermal infrared images have issues such as unclear detail levels, unobvious visual representation of temperature differences, and significant imaging noise impact, which are not conducive to defect detection and assessment. Therefore, it is necessary to enhance the thermal infrared image to better reflect temperature differences, which will facilitate subsequent ablation defect detection and assessment. The primary challenge lies in enhancing detail differences while effectively suppressing noise.

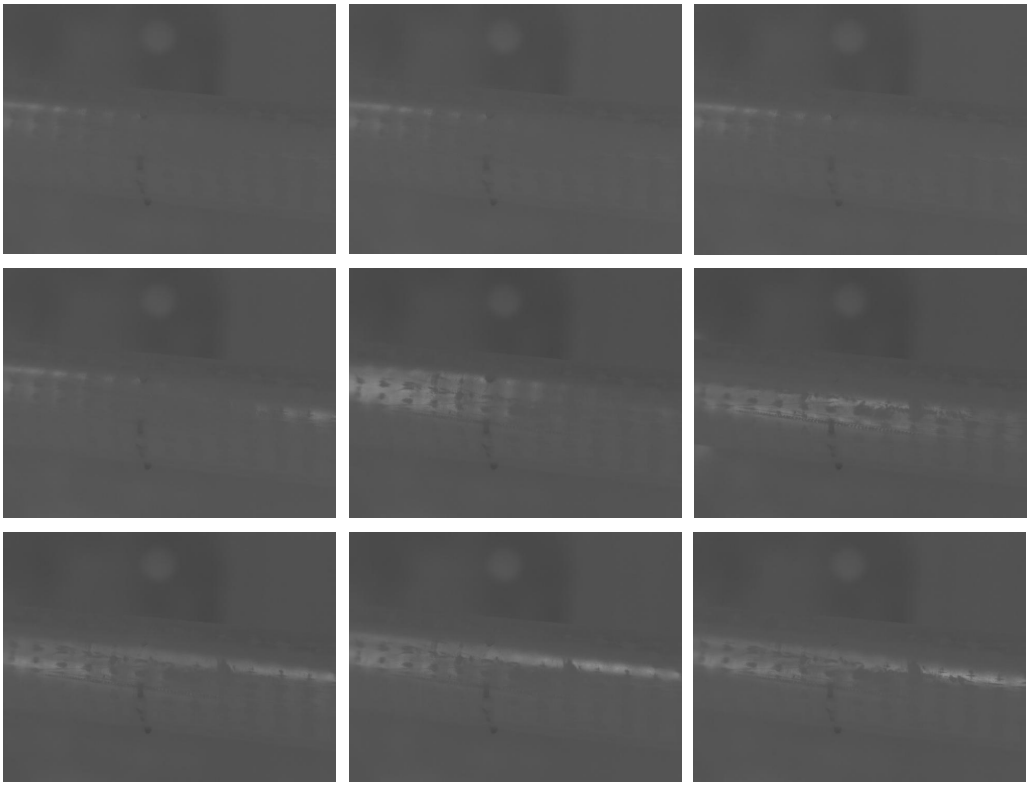

Figure 3. The images captured by an HIKMICRO infrared thermal imager. From **left** to **right**, from **top** to **bottom**, they are respectively referred to as Image 1 to Image 9.

3. Proposed Adaptive Enhancement Algorithm for Thermal Infrared Images

In response to the issues of high-voltage cable buffer layer ablation thermal infrared images, such as unclear detail hierarchy, unobvious visual representation of temperature differences, and significant imaging noise impact, this paper proposes an adaptive enhancement method, as shown in Figure 4, for thermal infrared images of high-voltage cable buffer layer ablation, which is based on background enhancement and detail denoising. The proposed method mainly includes five processing steps: adaptive image background and detail layer decomposition based on Average Gradient Weighted Guided Filtering (AGWGF), image background layer equalization enhancement based on improved Contrast Limited Adaptive Histogram Equalization (CLAHE), image detail layer denoising and stretching based on Adaptive Bilateral Filtering (ABF), image background and detail layer fusion stretching, and pseudo-color processing of the enhanced grayscale infrared images.

For a given grayscale infrared image of a cable, I, as shown in Figure 4, the background image I_b is first generated through AGWGF, and I_b is subtracted from the original image I to obtain the detail image I_d. For the background image I_b, it is enhanced using the improved CLAHE to obtain I_{bCLAHE}; for the detail image I_d, it is denoised and stretched using the improved ABF to obtain I_{dABFS}. Then, the enhanced grayscale thermal infrared image of the high-voltage cable I_e is obtained by fusing and stretching I_{bCLAHE} and I_{dABFS}. Finally, pseudo-color processing is performed on I_e to generate a pseudo-color thermal infrared image I_c.

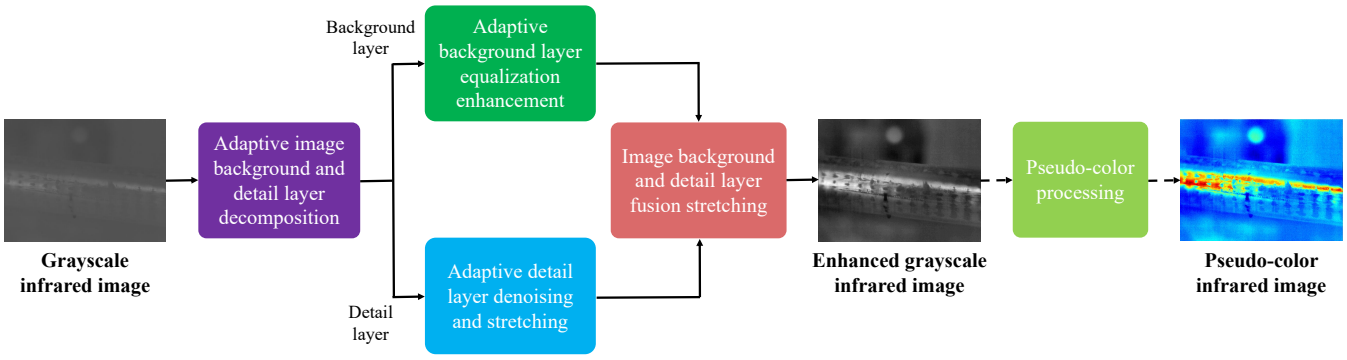

Figure 4. Flow chart of the proposed adaptive thermal infrared image enhancement method.

3.1. Adaptive Image Background and Detail Layer Decomposition Based on AGWGF

As shown in Figure 4, to avoid amplifying the noise in the enhanced infrared image, Average Gradient Weighted Guided Filtering (AGWGF) is proposed to separate the infrared image into background and detail layers and process them in different ways to achieve detail enhancement and noise suppression.

Guided filtering is an image filtering technique designed to smooth images while preserving details and edge information [32]. It requires the use of a guidance image for filtering, and in this paper the input image itself is used as the guidance image. Traditional guided filtering has parameters such as the filtering radius and intensity that need to be set manually; improper parameter selection may lead to the occurrence of halo effects [33]. This paper optimizes the regularization parameter and proposes AGWGF, which introduces the ratio of the current window's average gradient to the sum of the average gradients of all windows in the image as the edge-aware weight for the current pixel, effectively avoiding the halo artifacts in the filtered image.

Specifically, given the input image I and the guidance image p ($p = I$ in this work), the local linear relationship model between the output image of the guided filtering I_b and the guidance image p is:

$$I_{bi} = a_k p_i + b_k, \forall i \in \omega_k \tag{1}$$

where I_{bi} and p_i are the pixels at position i in I_b and p, respectively. a_k and b_k denote the local coefficients within a square window w_k centered at pixel point i. By calculating the correlation coefficients of the linear function for a_k and b_k, the following cost function is optimized within the window:

$$E(a_k, b_k) = \sum_{i \in \omega_k} ((a_k p_i + b_k - I_i)^2 + \frac{\varepsilon}{\varphi_i} a_k^2) \tag{2}$$

where I_i represents the pixel at position i in the image I. ε serves as the regularization parameter, which controls the degree of smoothing in the filtering process. ε is set to 600. φ_i is given by the following equation:

$$\varphi_i = \frac{1}{N} \sum_{j=1}^{N} \frac{g_i + \eta}{g_j + \eta} \tag{3}$$

where N represents the total number of pixels in the image. η is set to $(0.001T)^2$, where T represents the dynamic range of the image. g_i denotes the average gradient value within the window centered at pixel i, which is calculated as follows:

$$g_i = \frac{1}{n^2} \sum_{x=1}^{n} \sum_{y=1}^{n} \sqrt{[\frac{\partial I(x,y)}{\partial x}]^2 + [\frac{\partial I(x,y)}{\partial y}]^2} \tag{4}$$

where n is the side length of the square window w_k centered at the pixel i. $I(x, y)$ represents the pixel value of image I at the coordinates (x, y).

Based on the aforementioned equations, the solutions for a_k and b_k can be derived as follows:

$$a_k = \frac{\frac{1}{|\omega|}\sum_{i\in\omega_k} p_i I_i - \mu_k \bar{I}_k}{\sigma_k^2 + \frac{\varepsilon}{\varphi_i}} \tag{5}$$

$$b_k = \bar{I}_k - a_k \mu_k \tag{6}$$

where $|\omega|$ represents the number of pixels within the window ω_k; μ_k and ${\sigma_k}^2$ are the mean and variance, respectively, of the guidance image p within the window ω_k; and $\bar{I}_k$ denotes the mean of the input image I within the window ω_k.

Correspondingly, the output image I_{bi} is represented as:

$$I_{bi} = \bar{a}_i I_i + \bar{b}_i \tag{7}$$

where $\bar{a}_i$ and $\bar{b}_i$ represent the mean values of all a_k and b_k, respectively, within the square window ω_k centered at pixel i.

By applying AGWGF to the original image I, the background image I_b is obtained; subsequently, the detail image I_d is obtained by subtracting the background image from the original image. Here, the background layer I_b reflects the main body of the image, while the detail layer I_d contains more fine structures and noise.

3.2. Image Background Layer Equalization Enhancement Based on Improved CLAHE

Contrast Limited Adaptive Histogram Equalization (CLAHE) enhances image contrast by stretching the image's intensity level distribution and is an efficient method for image enhancement [29]. However, the performance of CLAHE is typically dependent on the selection of parameters, such as the size of the partitioned regions and the threshold of contrast limitation. This paper proposes an improvement to CLAHE by obtaining the threshold of contrast limitation based on the average gradient of image partitions, thereby achieving adaptive parameter selection when processing different images. The steps for the improved background layer enhancement algorithm are as follows:

(1) The background image I_b is divided into several equally sized, identically shaped, and non-overlapping fixed sub-blocks of size $m \times n$.

(2) Calculate the average gradient g_i within each image sub-block according to the following formula:

$$g_i = \frac{1}{mn}\sum_{x=1}^{m}\sum_{y=1}^{n}\sqrt{\left[\frac{\partial I_b(x,y)}{\partial x}\right]^2 + \left[\frac{\partial I_b(x,y)}{\partial y}\right]^2} \tag{8}$$

where m and n represent the length and width of the image sub-block, respectively, and $I_b(x, y)$ denotes the pixel value of the background image at the coordinates (x, y).

(3) The number of pixels in each image sub-block is evenly distributed across each intensity level, which is denoted as:

$$N_{aver} = \frac{N_{bx} N_{by}}{L} \tag{9}$$

where N_{bx} and N_{by} represent the number of pixels in the horizontal and vertical dimensions of the image sub-block, respectively; L denotes the number of distinct intensity levels present in the image sub-block i.

(4) The number of pixels associated with each intensity level within an image sub-block is constrained so as not to exceed the clipping threshold C_{limit}^i, formulated as:

$$C_{limit}^i = N_{aver} + N_{clip}^i (a g_i + b)(N_{bx} N_{by} - N_{aver}) \tag{10}$$

where N^i_{clip} is the clipping coefficient for the i-th image sub-block, where a and b are constants. N^i_{clip}, a, and b are set to 1, 1, and 4, respectively.

(5) For each image sub-block, the grayscale histogram is clipped, and the excess pixel count that is clipped off is evenly redistributed across all intensity levels. The average number of pixels redistributed to each intensity level is given by:

$$N_a = \frac{S_{clip}}{L} \tag{11}$$

where S_{clip} represents the total number of pixels that have been clipped. After the aforementioned redistribution, any remaining unallocated pixels are evenly distributed among the intensity levels that are less than C_{limit}, in a cyclic manner, until all remaining pixels are allocated.

(6) After applying contrast limitation to each image sub-block, histogram equalization is performed; further, bilinear interpolation is used to mitigate the block effect and enhance computational speed.

The improved CLAHE method is applied to the background image I_b, resulting in an enhanced background image I_{bCLAHE}.

3.3. Image Detail Layer Denoising and Stretching Based on ABF

Compared to traditional linear filters, the bilateral filter takes into account both the spatial distance between pixels and the differences in pixel values, thus better preserving image edge information and details during the denoising process [34]. To effectively filter out noise while retaining image details, this paper uses the improved Adaptive Bilateral Filter (ABF) to process the detail layer. First, the detail image is divided into blocks, and the average gradient of pixels within each block is calculated to determine the filtering parameters; then, different bilateral filters with varying parameters are applied to different blocks of the image for filtering.

Specifically, for a given detail image I_d, it is divided into several equally sized, identically shaped, and non-overlapping $m \times n$ image sub-blocks. ABF is performed on each image sub-block, and the pixel values of the output sub-block image are calculated using the following formula:

$$I^i_{dABF}(u) = \frac{1}{W} \sum_{v \in S} I^i_d(v) \cdot \omega^i(u, v) \tag{12}$$

where S represents the local neighborhood centered on the pixel point u; $I^i_d(v)$ denotes the pixel value of the sub-block I^i_d at the pixel point v; $\omega^i(u, v)$ is the weight between the pixels at u and v; and W is the normalization coefficient for the weights. The calculation formula for $\omega^i(u, v)$ is as follows:

$$\omega^i(u, v) = \exp\left(-\frac{\|u - v\|^2}{2{\delta^i_S}^2}\right) \cdot \exp\left(-\frac{\left\|I^i_d(u) - I^i_d(v)\right\|^2}{2{\delta^i_r}^2}\right) \tag{13}$$

$$\delta^i_S = a_S g_i \tag{14}$$

$$\delta^i_r = a_r g_i \tag{15}$$

where a_S and a_r are constants, and they are set to 75; δ^i_S is the standard deviation of the spatial Gaussian kernel applied to the i-th sub-block. A larger value of δ^i_S indicates that pixels spatially farther apart will also be considered for weight, resulting in a more pronounced smoothing effect on the image. δ^i_r is the standard deviation of the Gaussian kernel applied to the pixel values within the i-th sub-block. δ^i_r represents the degree of difference in pixel values. A smaller value of δ^i_r means that the filter is more sensitive to differences in pixel values, implying that only pixels with small value differences will be considered for weight calculation, thereby enriching the detail information in the image. g_i

is the average gradient of the i-th sub-block. After filtering, all sub-blocks are combined to obtain the denoised image I_{dABF}.

Furthermore, the denoised detail image I_{dABF} is stretched to obtain I_{dABFS}. Specifically, let the minimum and maximum values in image I_{dABF} be denoted by v_{min} and v_{max}, respectively. Correspondingly, the goal of stretching is to adjust the minimum and maximum values in image I_{dABFS} to αv_{min} and βv_{max}, which is achieved by the following transformation:

$$I_{dABFS} = \frac{I_{dABF} - v_{\min}}{v_{\max} - v_{\min}}(\beta v_{\max} - \alpha v_{\min}) + \alpha v_{\min} \tag{16}$$

where α and β are stretching parameters, and they are set to 6 and 3, respectively.

The improved bilateral filter is applied to the detail image I_d for denoising, and the resulting image I_{dABF} is stretched to obtain image I_{dABFS}.

3.4. Image Background and Detail Layer Fusion Stretching

The enhanced background image I_{bCLAHE} and the denoised and stretched detail image I_{dABFS} are fused to obtain image I_f:

$$I_f = I_{bCLAHE} + I_{dABFS} \tag{17}$$

Furthermore, I_f is stretched to obtain the enhanced grayscale infrared image I_e:

$$I_e = \frac{I_f - I_{f\_min}}{I_{f\_max} - I_{f\_min}}(R - 1) \tag{18}$$

where I_{f_max} and I_{f_min} represent the maximum and minimum grayscale values of image I_f, respectively; for an 8-bit image, R is set to 256.

3.5. Pseudo-Color Processing of Grayscale Infrared Images

Finally, pseudo-color processing is applied to the enhanced grayscale infrared image I_e to produce a pseudo-color image I_c, mapping pixels of different grayscale levels in the enhanced image to different colors to achieve a better visual effect and highlight the temperature distribution of the cable, facilitating the identification of heat-generating areas on the cable from the image. The proposed thermal infrared image enhancement method is summarized in Algorithm 1.

Algorithm 1 Adaptive Enhancement of Thermal Infrared Images

Require: The grayscale thermal infrared image I.
Ensure: The enhanced grayscale thermal infrared image I_e and the pseudo-color thermal infrared image I_c.
1: Decompose I to obtain the background layer I_b and the detail layer I_d based on AGWGF. (Equations (1)–(7))
2: Enhance the background layer I_b based on the improved CLAHE to generate I_{bCLAHE}. (Equations (8)–(11))
3: Enhance the detail layer I_d based on the improved ABF to generate I_{dABFS}. (Equations (12)–(16))
4: Fuse I_{bCLAHE} and I_{dABFS} to generate the enhanced grayscale thermal infrared image I_e. (Equations (17) and (18))
5: Perform pseudo-color processing on I_e to generate the pseudo-color thermal infrared image I_c.
6: **return** I_e and I_c.

4. Experimental Results and Analysis

In order to verify the effectiveness of the proposed adaptive enhancement method for high-voltage cable infrared images, the infrared images of the cable recorded by the HIKMICRO infrared thermal imager shown in Figure 3 are used as test images. The HE (Histogram Equalization) [35], MSR [36], CLAHE [29], and the method proposed in this paper are applied to enhance the test images, and a comparison and analysis are made in conjunction with subjective results and objective metrics. All experiments were conducted on a computer with an Intel(R) Core(TM) i7-6700K CPU (4.00 GHz) and 16 GB RAM using Python 3.11.

4.1. Subjective Results Comparison and Analysis

Figures 5–9 display the enhancement results of the infrared images of high-voltage cable buffer layer ablation. In each set of experimental result figures, the first column from top to bottom shows the original grayscale thermal infrared images of the high-voltage cable collected by the infrared thermal imager, as well as the grayscale thermal infrared images enhanced by HE [35], MSR [36], CLAHE [29], and the method proposed in this paper; the second column displays the pseudo-color image results corresponding to the grayscale thermal infrared images shown in the first column.

The results shown in Figures 5–9 indicate that the original grayscale cable images have low contrast and indistinct details, making it difficult to observe and analyze temperature differences, which leads to difficulties in assessing the ablation status of the buffer layer. The images enhanced with HE [35] exhibit excessive contrast, with details not standing out clearly, and there is a significant amount of noise. Compared to histogram equalization, both MSR [36] and CLAHE [29] enhance contrast while making details more prominent and reducing noise. The method proposed in this paper effectively removes noise while increasing contrast, providing the richest texture details and offering the best visual effect, allowing for a clearer observation of temperature changes and differences.

Regarding the pseudo-color images, the original cable pseudo-color images have low contrast, making it hard to distinguish details. In the pseudo-color images enhanced by the comparative methods, the high-temperature areas of the cable are not prominent, and the sense of hierarchy is poor. Compared to other algorithms, the pseudo-color images obtained by the method in this paper have richer texture details, with distinct temperature distribution levels, and the high-temperature areas of the cable are more prominent, allowing direct observation of the heat-generating areas and more closely resembling the temperature distribution in the original images.

4.2. Objective Metrics Comparison and Analysis

To compare the thermal infrared enhancement results more objectively and quantitatively, two common image quality assessment metrics including information entropy and average gradient are selected for comparison and analysis, with the experimental results shown in Tables 1 and 2.

Specifically, information entropy is a measure of the complexity or uncertainty of image content. Given an image I, its information entropy is defined as follows:

$$IE(I) = -\sum_{i=0}^{255} p_i \log_2 p_i \tag{19}$$

where p_i denotes the probability of the gray level i occurring in the image I. Information entropy is often used to assess the complexity or amount of information in an image; the higher the information entropy, the richer the information content of the image.

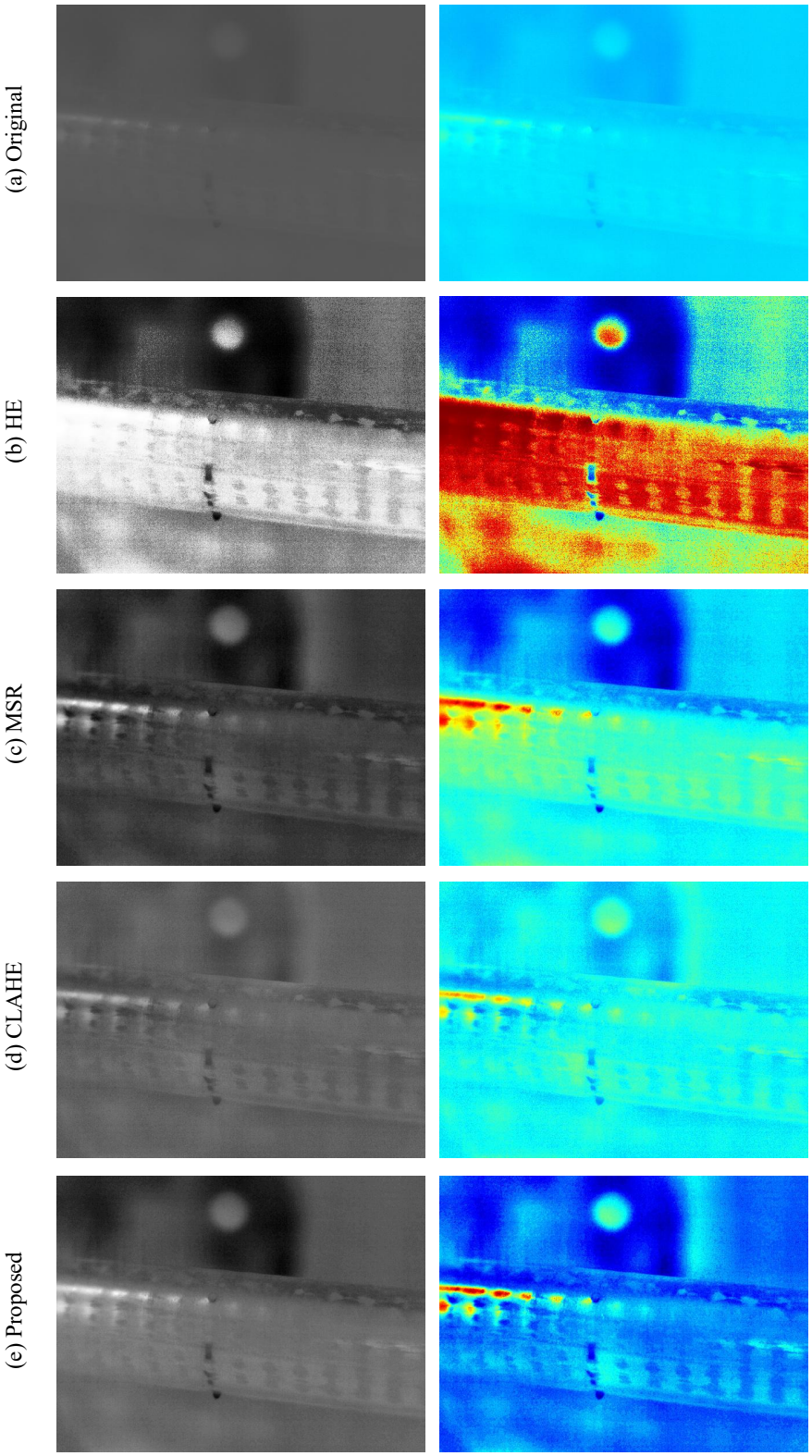

Figure 5. Visual quality comparison. The images in the first column are the original and enhanced thermal infrared images, and the corresponding pseudo-colored infrared images are shown in the second column.

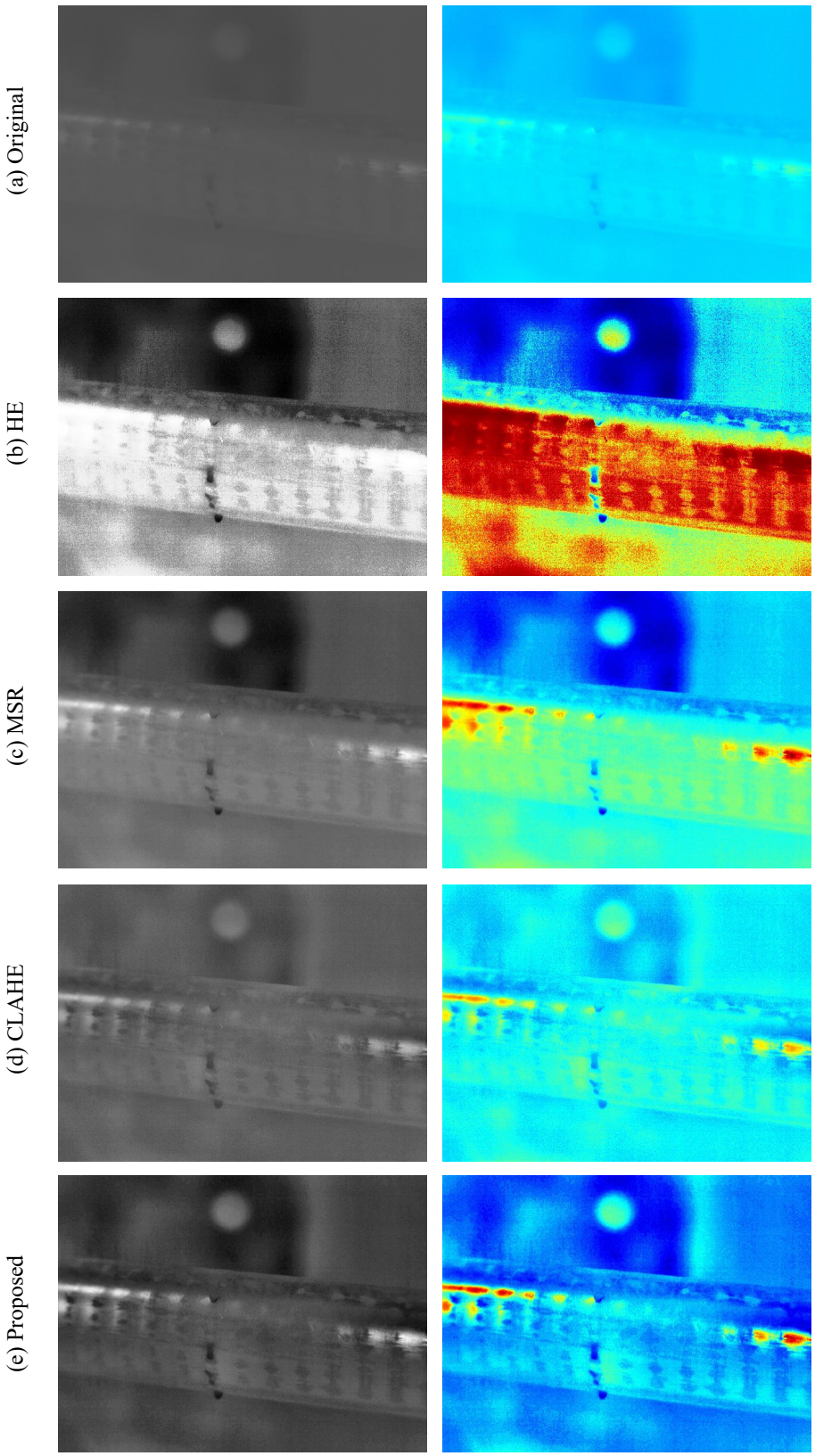

Figure 6. Visual quality comparison. The images in the first column are the original and enhanced thermal infrared images, and the corresponding pseudo-colored infrared images are shown in the second column.

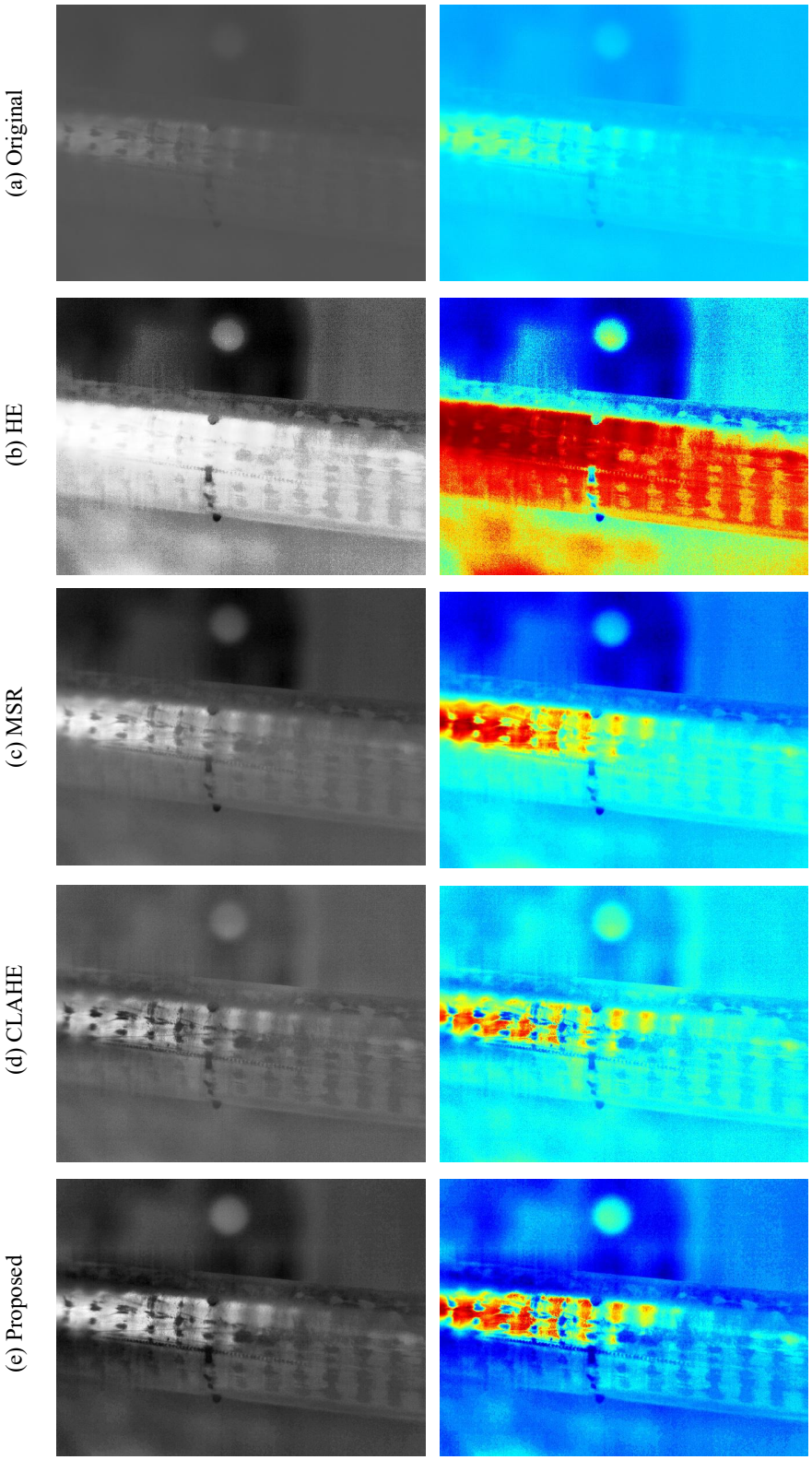

Figure 7. Visual quality comparison. The images in the first column are the original and enhanced thermal infrared images, and the corresponding pseudo-colored infrared images are shown in the second column.

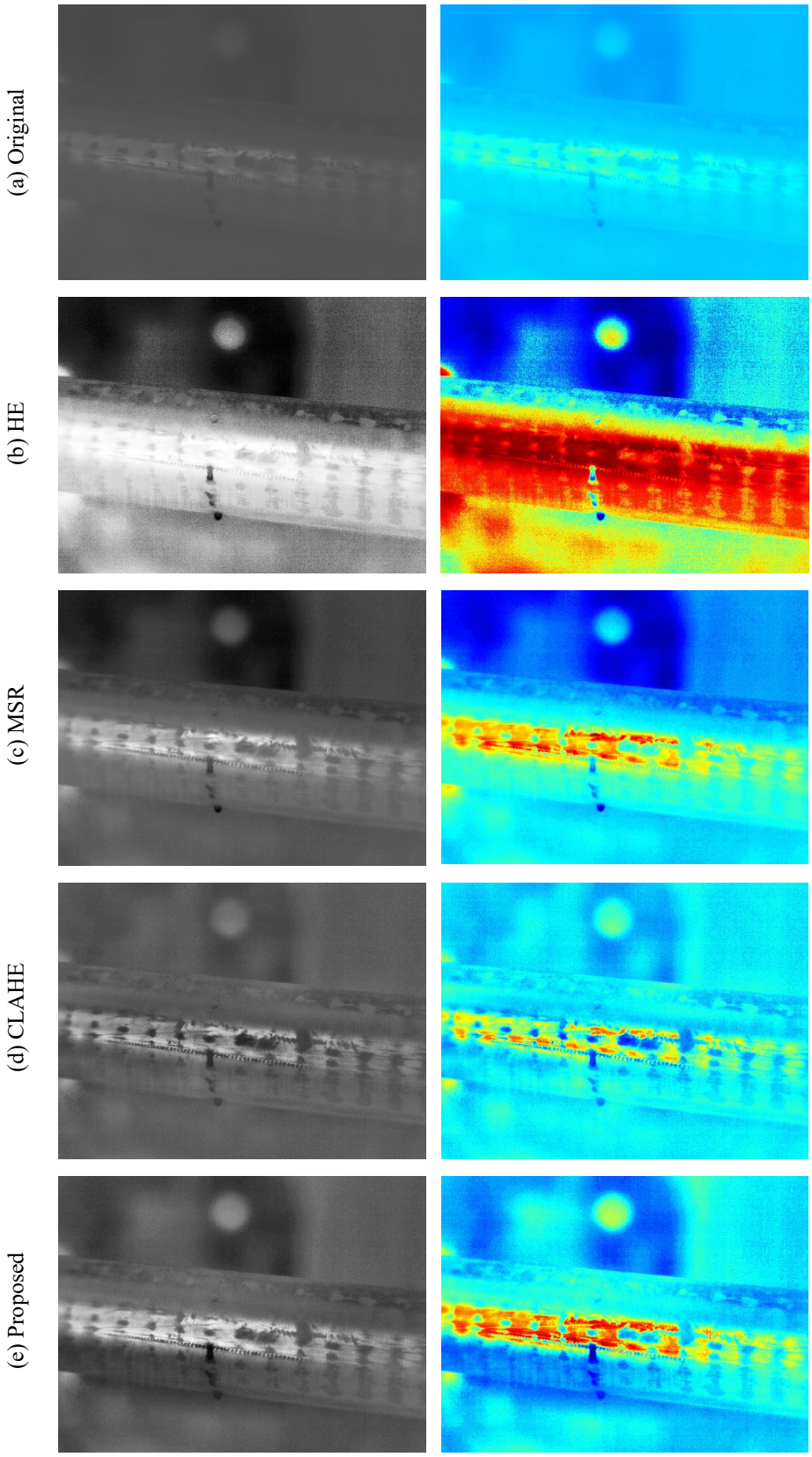

Figure 8. Visual quality comparison. The images in the first column are the original and enhanced thermal infrared images, and the corresponding pseudo-colored infrared images are shown in the second column.

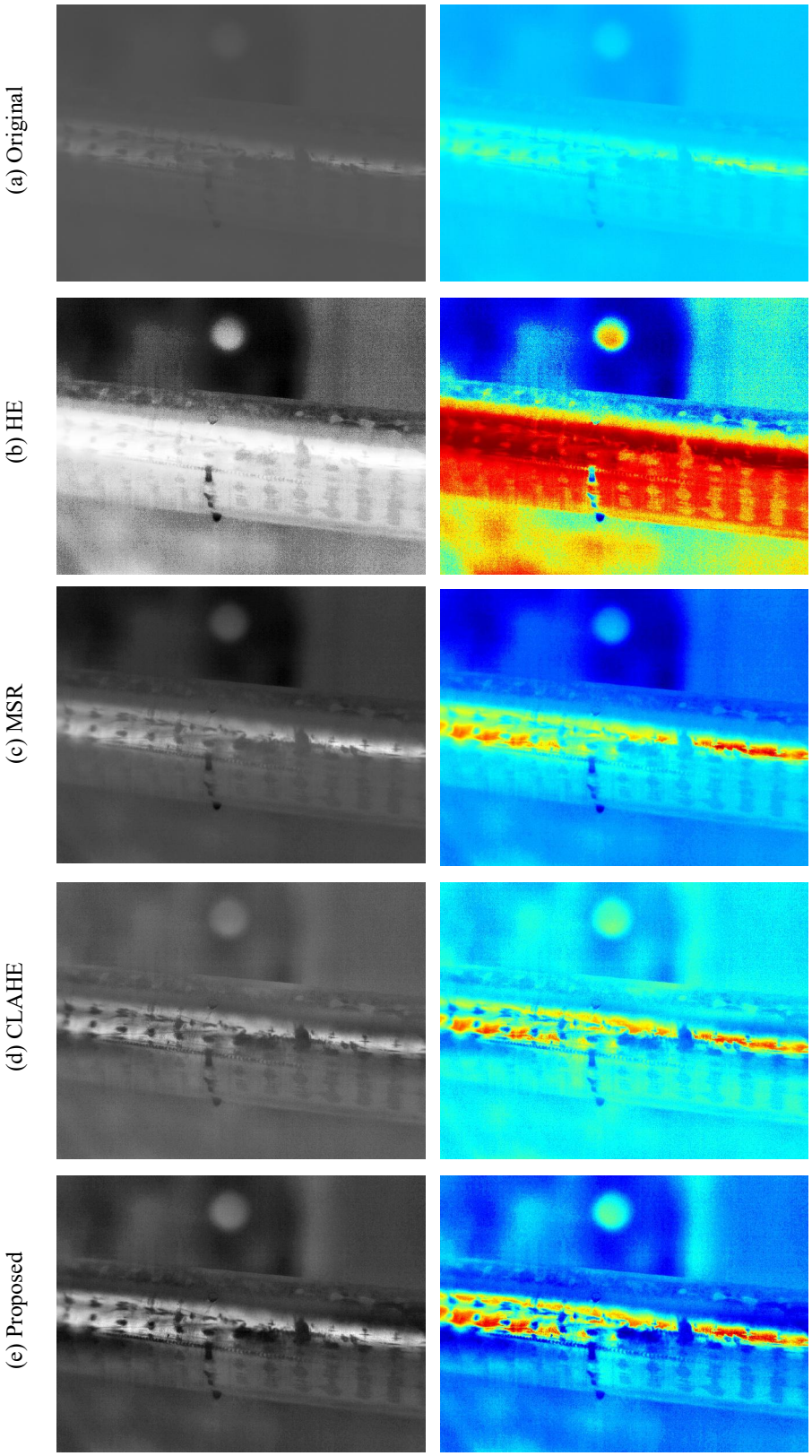

Figure 9. Visual quality comparison. The images in the first column are the original and enhanced thermal infrared images, and the corresponding pseudo-colored infrared images are shown in the second column.

The average gradient refers to the average degree of grayscale change between adjacent pixels in the image, which is defined as follows:

$$AG(I) = \frac{1}{MN}\sum_{x=1}^{M}\sum_{y=1}^{N}\sqrt{\left[\frac{\partial I(x,y)}{\partial x}\right]^2 + \left[\frac{\partial I(x,y)}{\partial y}\right]^2} \tag{20}$$

where M and N denote the length and width of I, respectively. The larger the average gradient, the more drastic the grayscale changes in the image, indicating the presence of more edges or details.

As shown in Table 1, for the nine high-voltage cable buffer layer ablation thermal infrared images, the enhancement results of the method proposed in this paper have a significantly higher information entropy compared to the original collected images and also outperform the results of other enhancement methods such as HE [35], MSR [36], and CLAHE [29]. This indicates that the enhancement results of the method proposed in this paper more clearly present the image detail structure, contain richer information, and thus can more directly and effectively reflect temperature changes and differences.

As demonstrated in Table 2, in terms of average gradient, the enhancement results of the method proposed in this paper are significantly superior to the original thermal infrared images as well as MSR [36] and CLAHE [29], highlighting the advantages of the enhancement outcomes of this method. HE [35] achieves the highest average gradient value, which can be attributed to the fact that the method does not take noise impact into consideration, and the enhancement process amplifies the noise, resulting in a noticeable presence of noise that leads to an increase in gradient values. The proposed method not only suppresses noise but also more clearly represents temperature changes and differences, which is conducive to improving the accuracy of cable condition assessment and monitoring.

To provide a more comprehensive evaluation of different methods, Table 3 further presents the processing time of various methods. The proposed method requires approximately 4.1 s per test image, which is slower than the compared methods. This is primarily due to the relatively more complex multi-stage framework of the proposed method, as illustrated in Figure 4. In this framework, the background and detail layers are decomposed and processed independently to prevent noise amplification during enhancement. The subjective and objective comparisons above indicate that the images enhanced by our proposed method display superior quality compared to those processed by competing methods, thereby validating the effectiveness of our framework.

Table 1. Comparison of information entropy scores between the proposed method and other methods.

	Original	**He [35]**	**MSR [36]**	**CLAHE [29]**	**Proposed**
Image 1	3.94	3.92	5.33	5.87	6.58
Image 2	3.92	3.89	5.32	5.84	6.59
Image 3	4.66	4.62	5.74	6.44	6.55
Image 4	4.63	4.57	5.84	6.39	6.47
Image 5	4.15	4.12	5.49	5.98	6.22
Image 6	4.49	4.44	5.80	6.23	6.36
Image 7	4.58	4.54	5.78	6.40	6.76
Image 8	4.53	4.49	5.85	6.25	6.72
Image 9	3.95	3.92	5.35	5.94	6.15
Average	4.32	4.28	5.61	6.15	6.49

Table 2. Comparison of average gradient scores between the proposed method and other methods.

	Original	He [35]	MSR [36]	CLAHE [29]	Proposed
Image 1	1.20	22.52	7.88	6.21	9.62
Image 2	1.24	24.01	8.05	6.38	10.05
Image 3	1.55	16.13	9.46	6.15	9.84
Image 4	1.51	16.93	9.30	5.67	9.41
Image 5	1.27	21.22	8.18	6.00	8.79
Image 6	1.55	18.30	9.19	5.31	10.26
Image 7	1.48	17.03	9.09	6.00	10.20
Image 8	1.49	16.94	8.85	5.39	10.03
Image 9	1.35	26.33	8.76	6.83	9.84
Average	1.40	19.93	8.75	5.99	9.78

Table 3. Comparison of running time between the proposed method and other methods.

	He [35]	MSR [36]	CLAHE [29]	Proposed
Running Time (s)	0.6	0.8	0.6	4.1

5. Conclusions

This paper proposes a thermal infrared image enhancement method for implementing temperature-based monitoring and assessment of high-voltage cable buffer layer ablation. The summary is as follows:

(1) High-voltage cable buffer layer ablation faults are associated with heat generation, and the method of monitoring and assessing the ablation status by combining infrared thermal imaging temperature measurement has the advantages of being convenient, efficient, and non-destructive.

(2) Test results indicate that the thermal infrared images of buffer layer ablation directly collected by infrared thermal imagers have issues with unobvious visual representation of temperature differences and interference from noise, which need to be improved by combining image enhancement techniques.

(3) Experimental results show that the proposed adaptive enhancement and pseudo-color processing method for thermal infrared images of high-voltage cable buffer layer ablation can effectively enhance image detail structure and suppress noise, more intuitively and clearly reflecting temperature changes and differences.

(4) Although the proposed method achieves excellent enhancement performance, it has certain limitations in terms of processing speed, and we will explore ways to improve processing efficiency in our future research.

Author Contributions: Conceptualization, H.Z., F.Z. and C.W.; methodology, H.Z., J.Z. and Q.H.; software, H.Z., J.Z. and Y.L.; validation, Y.L., Q.H. and K.Z.; formal analysis, H.Z., K.Z. and C.W.; investigation, H.Z., Y.L. and C.W.; resources, J.Z. and F.Z.; data curation, J.Z., Y.L. and K.Z.; writing—original draft preparation, H.Z.; writing—review and editing, Y.L., F.Z., K.Z. and C.W.; visualization, H.Z., Y.L. and Q.H.; supervision, J.Z., F.Z. and K.Z.; project administration, J.Z. and Q.H.; funding acquisition, J.Z. All authors have read and agreed to the published version of the manuscript.

Funding: This research was funded by the State Grid Corporation Science and Technology Project under Grant 5108-202218280A-2-353-XG.

Data Availability Statement: Data are only available on request due to restrictions (e.g., privacy, legal, or ethical reasons).

Conflicts of Interest: Authors Hao Zhan, Jing Zhang, Qinqing Huang and Chengde Wan were employed by the company State Grid Electric Power Research Institute. Authors Hao Zhan, Jing Zhang, Qinqing Huang and Chengde Wan were employed by the company Wuhan NARI Limited Liability Company of State Grid Electric Power Research Institute. The remaining authors declare that the research was conducted in the absence of any commercial or financial relationships that could be construed as a potential conflict of interest.

References

1. Choudhary, M.; Shafiq, M.; Kiitam, I.; Hussain, A.; Palu, I.; Taklaja, P. A review of aging models for electrical insulation in power cables. *Energies* **2022**, *15*, 3408. [CrossRef]
2. Zhu, G.; Zhou, K.; Lu, L.; Li, Y.; Xi, H.; Zeng, Q. Online monitoring of power cables tangent delta based on low-frequency signal injection method. *IEEE Trans. Instrum. Meas.* **2021**, *70*, 1–8. [CrossRef]
3. Song, Y.; Chen, W.; Wan, F.; Zhang, Z.; Du, L.; Wang, P.; Li, J.; Wu, Z.; Huang, H. Online multi-parameter sensing and condition assessment technology for power cables: A review. *Electr. Power Syst. Res.* **2022**, *210*, 108140. [CrossRef]
4. Song, P.; Meng, Z.; Li, X.; Zhu, M.; Yu, Y.; Fang, S. A case study on ablation breakdown of high voltage cable buffer layer. In Proceedings of the 2020 IEEE International Conference on High Voltage Engineering and Application (ICHVE), Beijing, China, 6–10 September 2020; pp. 1–4.
5. Zhang, H.; Gao, J.; Wu, K.; Zhao, G.; Sui, H.; Zhang, K.; Ge, Z.; Li, J. Effects of the inhomogeneous microstructures on buffer layer ablation failure in high voltage cables. *Eng. Fail. Anal.* **2023**, *152*, 107491. [CrossRef]
6. Tian, Y.; Zhu, G.; Miao, Q.; Huang, J.; Huang, X.; Li, S.; Li, L. Study on the Ablation Process and Failure Mechanism of the Buffer Layer in High-Voltage XLPE Cable. *Int. J. Electrochem. Sci.* **2024**, *19*, 100662. [CrossRef]
7. Chen, Y.; Zhou, K.; Kong, J.; Akram, S.; Ren, X.; Zhang, X.; Li, Y.; Zhao, Q. Hydrogen evolution and electromigration in the corrosion of aluminium metal sheath inside high-voltage cables. *High Volt.* **2022**, *7*, 260–268. [CrossRef]
8. Liu, Y.; Lian, R.; Chen, J.; Gao, X.; Ouyang, B.; Li, W. The formation mechanism of white substances on water-blocking buffer layer of HV XLPE cables. In Proceedings of the 2020 IEEE International Conference on High Voltage Engineering and Application (ICHVE), Beijing, China, 6–10 September 2020; pp. 1–4.
9. Chen, Y.; Hui, B.; Cheng, Y.; Hao, Y.; Fu, M.; Yang, L.; Hou, S.; Li, L. Failure investigation of buffer layers in high-voltage XLPE cables. *Eng. Fail. Anal.* **2020**, *113*, 104546. [CrossRef]
10. Hui, B.; Cheng, Y.; Huang, J.; Hou, S.; Zhu, W.; Zhao, P. The formation mechanism of white powder in cable water blocking tape and its influence on volume resistivity and thermal conductivity. In Proceedings of the 22nd International Symposium on High Voltage Engineering (ISH 2021), Xi'an, China, 21–26 November 2021.
11. Jiang, L.; Xin, Y.; Yan, W.; Zhao, X.; Yao, R.; Shen, Z.; Gao, J.; Zhong, L.; Wald, D.F.; Ren, Z. Study on ablation between metal sheath and buffer layer of high voltage XLPE insulated power cable. In Proceedings of the 2019 2nd International Conference on Electrical Materials and Power Equipment (ICEMPE), Guangzhou, China, 7–10 April 2019; pp. 372–375.
12. Xin, Y.; Jiang, L.; Zhao, X.; Li, W.; Gao, J.; Xi, B.; Zhong, L.; Xia, L. Cause analysis of aging ablation on sheath of 110 kV single core high voltage cable. In Proceedings of the 2019 IEEE Conference on Electrical Insulation and Dielectric Phenomena (CEIDP), Richland, WA, USA, 20–23 October 2019; pp. 162–165.
13. Zhang, T.; Yang, F.; Zheng, M.; Huang, J.; Zhou, K. Research on ablation characteristics of XLPE Cable buffer layer based on electrothermal coupling method. In Proceedings of the 18th International Conference on AC and DC Power Transmission (ACDC 2022), Online, 2–3 July 2022.
14. Li, N.; Zeng, D.; Zhao, Y.; Wang, J.; Wang, B. A Convolutional Neural Network-Based Defect Recognition Method for Power Insulator. *Processes* **2024**, *12*, 2129. [CrossRef]
15. Gou, M.; Tang, H.; Song, L.; Chen, Z.; Yan, X.; Zeng, X.; Fu, W. Research on Defect Diagnosis of Transmission Lines Based on Multi-Strategy Image Processing and Improved Deep Network. *Processes* **2024**, *12*, 1832. [CrossRef]
16. Versaci, M.; Angiulli, G.; La Foresta, F.; Crucitti, P.; Laganá, F.; Pellicanó, D.; Palumbo, A. Innovative soft computing techniques for the evaluation of the mechanical stress state of steel plates. In Proceedings of the International Conference on Applied Intelligence and Informatics, Reggio, Italy, 1–3 September 2022; Springer: Berlin/Heidelberg, Germany, 2022; pp. 14–28.
17. Li, H.; Yi, Z.; Mei, L.; Duan, J.; Sun, K.; Li, M.; Yang, W.; Wang, Y. SCFNet: Lightweight Steel Defect Detection Network Based on Spatial Channel Reorganization and Weighted Jump Fusion. *Processes* **2024**, *12*, 931. [CrossRef]
18. Liu, M.; Zhang, M.; Chen, X.; Zheng, C.; Wang, H. YOLOv8-LMG: An Improved Bearing Defect Detection Algorithm Based on YOLOv8. *Processes* **2024**, *12*, 930. [CrossRef]
19. Versaci, M.; Angiulli, G.; Crucitti, P.; De Carlo, D.; Laganà, F.; Pellicanò, D.; Palumbo, A. A fuzzy similarity-based approach to classify numerically simulated and experimentally detected carbon fiber-reinforced polymer plate defects. *Sensors* **2022**, *22*, 4232. [CrossRef] [PubMed]
20. Deng, D.; Liu, Z.; Lv, P.; Sheng, M.; Zhang, H.; Yang, R.; Shi, T. Defect Detection in Food Using Multispectral and High-Definition Imaging Combined with a Newly Developed Deep Learning Model. *Processes* **2023**, *11*, 3295. [CrossRef]
21. Wu, Z.; Lai, Q.; Zhou, W.; Liu, X.; Chen, J.; Hu, L.; Hao, Y.; Liu, G. Analysis of influencing factors on buffer layer discharge for high-voltage XLPE cable. *IET Gener. Transm. Distrib.* **2022**, *16*, 4142–4157. [CrossRef]

22. Liu, S.; Zhang, L.; Duan, J.; Zhang, J.; Huang, F.; Duan, X.I.; Zeng, Z. X-Ray Digital Image Advanced Processing and Buffer Layer Defect Intelligent Identification of Power Cable. *J. Phys. Conf. Ser.* **2020**, *1601*, 052028. [CrossRef]
23. Huang, Z.; Lu, F.; Tong, Y.; Shi, T. Technology for the detection of ablation defects in buffer layers of high-voltage cables. *IEEE Access* **2022**, *10*, 92843–92853. [CrossRef]
24. He, W.; Wu, Z.; Wu, H.; Bao, J.; Zhou, X.; Zhou, Q.; Zhang, H. The simulation research on propagation characteristics of acoustic signal generated by buffer layer ablation defects in high voltage cable. In Proceedings of the 2021 6th Asia Conference on Power and Electrical Engineering (ACPEE), Chongqing, China, 8–11 April 2021; pp. 237–241.
25. Liu, J.; Ma, M.; Liu, X.; Xu, H. High-Voltage Cable Buffer Layer Ablation Fault Identification Based on Artificial Intelligence and Frequency Domain Impedance Spectroscopy. *Sensors* **2024**, *24*, 3067. [CrossRef] [PubMed]
26. Wang, J.; Xiao, X.; Fan, Y.; Cai, L.; Tong, Y.; Rao, Z.; Huang, Z. Interface defect detection for composite insulators based on infrared thermography axial temperature method. *Infrared Phys. Technol.* **2018**, *93*, 232–239. [CrossRef]
27. He, S.; Yang, D.; Li, W.; Xia, Y.; Tang, Y. Detection and fault diagnosis of power transmission line in infrared image. In Proceedings of the 2015 IEEE International Conference on Cyber Technology in Automation, Control, and Intelligent Systems (CYBER), Shenyang, China, 8–12 June 2015; pp. 431–435.
28. Cong, S.; Pu, H.; Yao, F. Review on application of infrared detection technology in state detection of electrical equipment. In Proceedings of the 16th Annual Conference of China Electrotechnical Society: Volume II, Beijing, China, 24–26 September 2021; Springer: Singapore, 2022; pp. 1254–1261.
29. Zuiderveld, K. Contrast limited adaptive histogram equalization. In *Graphics Gems IV*; Morgan Kaufmann: Burlington, MA, USA, 1994; pp. 474–485.
30. Zhou, J.; Cunha, A.L.; Do, M.N. Nonsubsampled contourlet transform: construction and application in enhancement. In Proceedings of the IEEE International Conference on Image Processing 2005, Genoa, Italy, 11–14 September 2005; Volume 1, pp. I–469.
31. Yuan, L.T.; Swee, S.K.; Ping, T.C. Infrared image enhancement using adaptive trilateral contrast enhancement. *Pattern Recognit. Lett.* **2015**, *54*, 103–108. [CrossRef]
32. He, K.; Sun, J.; Tang, X. Guided image filtering. *IEEE Trans. Pattern Anal. Mach. Intell.* **2012**, *35*, 1397–1409. [CrossRef]
33. Li, Z.; Zheng, J.; Zhu, Z.; Yao, W.; Wu, S. Weighted guided image filtering. *IEEE Trans. Image Process.* **2014**, *24*, 120–129. [PubMed]
34. Tomasi, C.; Manduchi, R. Bilateral filtering for gray and color images. In Proceedings of the Sixth International Conference on Computer Vision, Bombay, India, 4–7 January 1998; pp. 839–846.
35. Gonzales, R.C.; Wintz, P. *Digital Image Processing*; Addison-Wesley Longman Publishing Co., Inc.: Boston, MA, USA, 1987.
36. Rahman, Z.u.; Jobson, D.J.; Woodell, G.A. Multi-scale retinex for color image enhancement. In Proceedings of the 3rd IEEE International Conference on Image Processing, Lausanne, Switzerland, 16–19 September 1996; Volume 3, pp. 1003–1006.